JOURNAL OF COMPUTATIONAL PHYSICS 84, 145-173 (1989)

A High-Resolution TVD Finite Volume Scheme for the Euler Equations in Conservation Form

J. C. T. WANG AND G. F. WIDHOPF

The Aerospace Corporation, El Segundo, California 90245

Received January 20, 1988; revised August 22, 1988

A finite-volume numerical algorithm using nonuniformly distributed skewed, quadrilateral cells is developed to solve the Euler equations in conservation form. Fluxes across the cell boundaries are computed using the total variation diminishing (TVD) methodology developed by Harten. Proof of the TVD property for nonuniform grid systems and a truncation error analysis are presented along with a discussion of the treatment of boundary conditions. Four test cases are given to examine the efficacy of the present scheme using a system of skewed and nonuniform cells. The excellent agreement of the numerical results with exact solutions and carefully designed experiments demonstrates the ability of the present scheme to accurately resolve complicated wave developments and interactions using highly nonuniform multiblock zonal cell distributions.

I. INTRODUCTION

Analysis of high speed flow problems invariably involves the resolution of shock waves internal to the computational domain. For complicated geometries, there may be multiple interactions of weak and strong shock waves, expansion waves, and contact discontinuities which make an accurate evaluation of the local flow properties very difficult.

The development of TVD [1–3] numerical schemes has been a significant milestone for attaining accurate local resolution of these discontinuities and their interactions in a few grid locations without spurious oscillations. These schemes have now been widely applied for numerical calculation of inviscid flow problems (e.g., Refs. 4–6) using finite difference techniques.

The purpose of this paper is to extend these TVD ideas [3] to finite volume techniques, since these latter numerical schemes allow for a direct treatment of complicated multidimensional geometries associated with practical systems. They also allow for the use of nonuniform global or localized multiblock grid specifications which may be very necessary to efficiently resolve the flow patterns for complicated practical configurations.

Specifically, the TVD methodology developed by Harten [3] for uniform mesh finite difference schemes will be modified and applied to the evaluation of the flux

0021-9991/89 $3.00

between skewed finite-volumes (cells) arbitrarily distributed in the computational domain. This type of cell distribution and the communication between *multiple* adjoining cells can be viewed in the context of local zonal multiblock gridding. These localized nonuniform cell specifications do not influence cell distributions in other areas of the computational domain as can be the case for curvilinear coordinates or some transformation techniques which require cell nodal connectivity. The goal is to be able to solve for the inviscid flow over complex configurations by this second order, finite volume TVD scheme.

In Section II, the basic discrete difference equations are developed for the finite-volume scheme using skewed cells. The reader is referred to Harten's [3] original paper for theoretical details of his basic scheme; however, the theory necessary for the extension of the technique to this finite volume application is contained herein. Also included is proof of the retention of the TVD properties in nonuniform grid systems and a truncation error analysis (Appendices A and B). Four numerical experiments are presented in Section III. Their purpose is to demonstrate the efficacy of the scheme using skewed and/or nonuniform cells in the computational domain. These problems demonstrate the ability of the finite volume technique to resolve complicated wave development and interactions in one and two dimensions as well as in very complicated axisymmetric flow problems.

II. Discrete Finite-Volume Scheme

A. *Differential Equations*

Consider the Euler equations in "conservation" form for 2-dimensional and axisymmetric flow problems

$$\frac{\partial U}{\partial t}+\frac{\partial F}{\partial x}+\frac{\partial G}{\partial y}=S, \tag{1}$$

where

$$U=\begin{bmatrix}\rho y^{\alpha}\\ \rho u y^{\alpha}\\ \rho v y^{\alpha}\\ \rho e y^{\alpha}\end{bmatrix};\qquad F=\begin{bmatrix}\rho u y^{\alpha}\\ (p+\rho u^2)\, y^{\alpha}\\ \rho u v y^{\alpha}\\ \rho u(e+p/\rho)\, y^{\alpha}\end{bmatrix};$$

$$G=\begin{bmatrix}\rho v y^{\alpha}\\ \rho u v y^{\alpha}\\ (p+\rho v^2)\, y^{\alpha}\\ \rho v(e+p/\rho)\, y^{\alpha}\end{bmatrix};\qquad S=\begin{bmatrix}0\\ 0\\ \alpha p\\ 0\end{bmatrix};$$

and $\alpha=0, 1$ for 2-dimensional and axisymmetric problems, respectively; ρ is the density; p is the pressure; u and v are the velocity components in the x- and y-direc-

tions, respectively; and e is the total energy per unit mass. For a polytropic gas, e is related to p by the equation of state

$$p = (\gamma - 1)\,\rho[e - (u^2 + v^2)/2]$$

B. *Difference Equations*

For a finite volume scheme, the difference equations are generated by integrating Eqs. (1) over a cell volume V whose boundaries can be time dependent. However, only stationary boundaries are considered here, and the reader is referred to Ref. [7] for the treatment of the more general case including moving boundaries within the computational domain.

Therefore, the integrated form of Eqs. (1) is

$$\frac{\partial}{\partial t}\iint_V U\,dx\,dy + \iint_V \left[\frac{\partial F}{\partial x} + \frac{\partial G}{\partial y}\right] dx\,dy = \iint_V S\,dx\,dy, \tag{2}$$

where the double integration represents a volume integral, since the integration in the third dimension has already been performed. When Gauss' theorem is applied, the second term in Eq. (2) can be converted to a surface integral representing the fluxes across a cell boundary

$$\iint_V \nabla \cdot \mathbf{V}\,dx\,dy = \int_A \mathbf{V} \cdot \hat{N}\,dA, \tag{3}$$

where $\mathbf{V} \equiv F\hat{i} + G\hat{j}$, A is the complete boundary of V, and $\hat{N}$ is the unit outward normal of dA.

Using an explicit first-order-accurate time differencing scheme, for a quadrilateral cell of skewed shape as shown in Fig. 1a, we can write the difference equations for Eqs. (1) as

$$\text{mass:} \quad \rho_{i,j}^{n+1} = \rho_{i,j}^n - \frac{\Delta t}{\Delta V_{i,j}} \sum_{k=1}^{4} \{(\rho u)_k^n A_k N_{kx} + (\rho v)_k^n A_k N_{ky}\} \tag{4a}$$

$$x\text{-momentum:} \quad (\rho u)_{i,j}^{n+1} = (\rho u)_{i,j}^n - \frac{\Delta t}{\Delta V_{i,j}} \sum_{k=1}^{4} \{(\rho u^2 + p)_k^n A_k N_{kx} + (\rho uv)_k^n A_k N_{ky}\} \tag{4b}$$

$$y\text{-momentum:} \quad (\rho v)_{i,j}^{n+1} = (\rho v)_{i,j}^n - \frac{\Delta t}{\Delta V_{i,j}} \sum_{k=1}^{4} \{(\rho uv)_k^n A_k N_{kx} + (\rho v^2 + p)_k^n A_k N_{ky} + \alpha p_{i,j}^n A_k N_{ky}\} \tag{4c}$$

$$\text{Energy:} \quad (\rho e)_{i,j}^{n+1} = (\rho e)_{i,j}^n - \frac{\Delta t}{\Delta V_{i,j}} \sum_{k=1}^{4} \{[(p/\rho + e)\,\rho u]_k^n A_k N_{kx} + [(p/q + e)\,\rho v]_k^n A_k N_{ky}\}, \tag{4d}$$

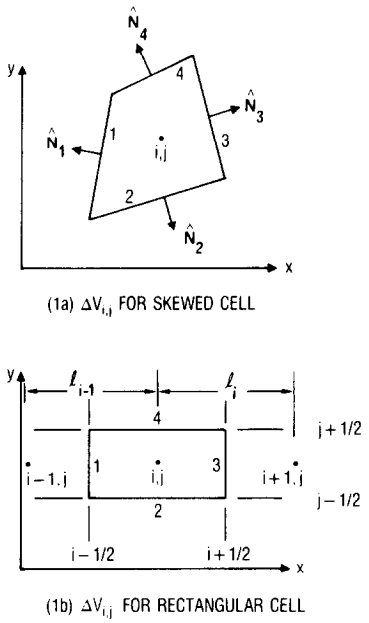

(1a) $\Delta V_{i,j}$ FOR SKEWED CELL

(1b) $\Delta V_{i,j}$ FOR RECTANGULAR CELL

FIG. 1. Finite volume cell geometries.

where the superscript n represents the time step; subscripts i and j identify the cell; $\Delta V_{i,j}$ is the volume of cell i, j; and the subscript k outside a parenthesis or a bracket indicates that the enclosed dependent variables (physical fluxes) are to be evaluated on the surface k. Assumptions implicit in the derivation of these equations are that the volume integration is well approximated using the cell center value and the flux properties are assumed constant over a given surface.

Use of rectangular cells aligned with the coordinate directions as shown in Fig. 1b simplifies the evaluation of the flux terms and the cell description. However, there is a significant loss of flexibility. A prominent focus of the present work, therefore, is to retain the geometric flexibility shown in Fig. 1a in order to handle complex configurations not readily amenable to transformation techniques. This arbitrary distribution of cells can be interpreted as a general zonal grid specification.

The solution of the above system of difference Eqs. (4) yields the flow variables ρ, u, v, and e at the center of a cell and at time t^{n+1}, once the fluxes across the cell boundaries are evaluated. A number of schemes can be used to accomplish this.

The Godunov [8] method, and variants thereof [1, 9] has been used in the past (among others) to evaluate these flux terms, since its physical analogy allows it to readily handle flows with shocks and contact discontinuities. However, due to the diffusive nature of the original Godunov method, discontinuities are usually smeared, sometimes excessively. This situation becomes worse when the flow involves interactions of various strong waves and contact discontinuities.

In this paper, the TVD methodology developed by Harten [3] for finite difference schemes is modified and applied to numerically evaluate the flux terms. For the sake of clarity, the application of the algorithm will be explained for a nonuniform distribution of rectangular cells aligned with the coordinate directions. Both the axisymmetric case and skewed cells will be discussed later in this section.

Following Harten, the numerical approximation for Eqs. (1) is

$$U_{i,j}^{n+1} = U_{i,j}^{n} - [\lambda_i(\bar{F}_{i+1/2,j}^{n} - \bar{F}_{i-1/2,j}^{n}) + \lambda_j(\bar{G}_{i,j+1/2}^{n} - \bar{G}_{i,j-1/2}^{n})], \tag{5}$$

where $\lambda_i = \Delta t/\Delta x_i$; $\lambda_j = \Delta t/\Delta y_j$; and the numerical flux terms $\bar{F}_{i+1/2,j}^{n}$ and $\bar{F}_{i-1/2,j}^{n}$ are written in the form

$$\bar{F}_{i+1/2,j} = \frac{1}{2}\left\{F(U_{i,j}) + F(U_{i+1,j}) - [F(U_{i+1,j}) - F(U_{i,j})]\frac{\Delta x_{i+1} - \Delta x_i}{\Delta x_{i+1} + \Delta x_i} - \frac{1}{\lambda_i}\sum_{k=1}^{4}\beta_{i+1/2,j}^{k} R_{i+1/2,j}^{k}\right\} \tag{6a}$$

$$\bar{F}_{i-1/2,j} = \frac{1}{2}\left\{F(U_{i,j}) + F(U_{i-1,j}) - [F(U_{i,j}) - F(U_{i-1,j})]\frac{\Delta x_i - \Delta x_{i-1}}{\Delta x_i + \Delta x_{i-1}} - \frac{1}{\lambda_i}\sum_{k=1}^{4}\beta_{i-1/2,j}^{k} R_{i-1/2,j}^{k}\right\}. \tag{6b}$$

These equations reduce to Harten's uniform grid spacing form as $\Delta x_i \to \Delta x_{i-1}$. In Appendix A, it is proven that the TVD property is preserved for a nonuniform cell specification. It is shown in Appendix B that the scheme retains its second-order accuracy, if the variation of the cell distribution is smoother than an algebraic distribution of power greater than 1. (For the definition of an algebraic distribution, see Ref. [10].)

The last term in Eqs. (6) represents the combination of the numerical viscosity and artificial compression. The method adopted to construct this latter term is essentially the one referred to as UTL1C in Ref. [3].

Equation (6) represents the numerical evaluation of the fluxes in the x-direction; consequently, j is kept constant. In the following, we shall omit the j index. In Eq. (6), the vector $\beta_{i+1/2}$ is given by

$$\beta_{i+1/2}^{k} = Q^{k}(\nu_{i+1/2}^{k} + \gamma_{i+1/2}^{k})\,\alpha_{i+1/2}^{k} - (g_i^{k} + g_{i+1}^{k}), \tag{7a}$$

where

$$v^k_{i+1/2} = \lambda_i a^k_{i+1/2} \tag{7b}$$

$$\begin{aligned} a^1_{i+1/2} &= \hat{u}_{i+1/2} - \hat{c}_{i+1/2}, \qquad a^2_{i+1/2} = \hat{u}_{i+1/2} \\ a^3_{i+1/2} &= \hat{u}_{i+1/2} + \hat{c}_{i+1/2}, \qquad a^4_{i+1/2} = \hat{u}_{i+1/2} \end{aligned} \tag{7c}$$

and

$$\begin{aligned} \hat{u}_{i+1/2} &= \langle \rho^{1/2} u \rangle / \langle \rho^{1/2} \rangle \\ \hat{c}_{i+1/2} &= \{(\gamma - 1)[\hat{H}_{i+1/2} - \tfrac{1}{2}(\hat{u}^2_{i+1/2} + \hat{v}^2_{i+1/2})]\}^{1/2}. \end{aligned} \tag{7d}$$

Here, $\langle b \rangle$ denotes an arithmetic average

$$\langle b \rangle = \tfrac{1}{2}(b_i + b_{i+1}), \tag{7e}$$

H is the enthalpy given by

$$H = \gamma p/(\gamma - 1)\,\rho + \tfrac{1}{2}(u^2 + v^2), \tag{8}$$

and γ is the ratio of specific heats which should not be confused with $\gamma^k_{i+1/2}$. In Eq. (7b), $a^k_{i+1/2}$, $k = 1, \ldots, 4$, are eigenvalues of the Jacobian $A = \partial F/\partial U$ expressed in terms of Roe's [9] averaged quantities. The $R^k_{i+1/2}$ is the kth column of the right eigenvector where

$$R_{i+1/2} = \begin{bmatrix} 1 & 1 & 1 & 0 \\ \hat{u}_{i+1/2} - \hat{c}_{i+1/2} & \hat{u}_{i+1/2} & \hat{u}_{i+1/2} + \hat{c}_{1+1/2} & 0 \\ \hat{v}_{i+1/2} & \hat{v}_{i+1/2} & \hat{v}_{i+1/2} & 1 \\ \hat{H}_{i+1/2} - \hat{u}_{1+1/2}\hat{c}_{i+1/2} & (\hat{u}^2_{i+1/2} + \hat{v}^2_{i+1/2})/2 & \hat{H}_{i+1/2} + \hat{u}_{i+1/2}\hat{c}_{i+1/2} & \hat{v}_{i+1/2} \end{bmatrix}, \tag{9}$$

where $\hat{v}_{i+1/2} = \langle \rho^{1/2} v \rangle / \langle \rho^{1/2} \rangle$.

The functional form of the numerical viscosity term, Q, is given by

$$Q(x) = \begin{cases} \tfrac{1}{2}(x^2/\varepsilon + \varepsilon) & \text{for} \quad |x| \leqslant \varepsilon \\ |x| & \text{for} \quad |x| > \varepsilon, \end{cases} \tag{10}$$

where ε is a constant between 0.20 and 0.5. The components of the vector $\alpha_{i+1/2}$ are defined as

$$\begin{aligned} \alpha^1_{i+1/2} &= \tfrac{1}{2}(C_1 - C_2), \qquad \alpha^2_{i+1/2} = [\rho]_{i+1/2} - C_1 \\ \alpha^3_{i+1/2} &= \tfrac{1}{2}(C_1 + C_2) \\ \alpha^4_{i+1/2} &= [\rho v]_{i+1/2} - \hat{v}_{i+1/2}[\rho]_{i+1/2}, \end{aligned} \tag{11}$$

where $[b]_{i+1/2} \equiv b_{i+1} - b_i$ and

$$\begin{aligned} C_1 &= (\gamma - 1)\{[\rho e]_{i+1/2} + \tfrac{1}{2}(\hat{u}^2_{i+1/2} + \hat{v}^2_{i+1/2})[\rho]_{i+1/2} \\ &\quad - \hat{u}_{i+1/2}[\rho u]_{i+1/2} - \hat{v}_{i+1/2}[\rho v]_{i+1/2}\}/\hat{c}^2_{i+1/2} \\ C_2 &= \{[\rho u]_{i+1/2} - \hat{u}_{i+1/2}[\rho]_{i+1/2}\}/\hat{c}_{i+1/2}. \end{aligned}$$

The vector, g_i, which includes the artificial compression factor, θ, is given by

$$\begin{aligned} g_i^k &= \bar{g}_i^k + \theta_i \bar{\bar{g}}_i^k \\ \bar{g}_i^k &= S_{i+1/2}^k \max[0, \min(|\tilde{g}_{i+1/2}^k|, \tilde{g}_{i-1/2}^k S_{i+1/2}^k)], \end{aligned} \tag{12}$$

where

$$\tilde{g}_{i+1/2}^k = \tfrac{1}{2}[Q^k(v_{i+1/2}^k) - (v_{i+1/2}^k)^2]\, \alpha_{i+1/2}^k$$

and

$$S_{i+1/2}^k = \operatorname{sgn}(\tilde{g}_{i+1/2}^k) \tag{13a}$$

$$\begin{aligned} \gamma_{i+1/2}^k &= (\bar{g}_{i+1}^k - \bar{g}_i^k)/\alpha_{i+1/2}^k, && \text{when } \alpha_{i+1/2}^k \neq 0 \\ &= 0 && \text{when } \alpha_{i+1/2}^k = 0 \end{aligned} \tag{13b}$$

$$\bar{\bar{g}}_i^k = S \max[0, \min(S\sigma_{i-1/2}\alpha_{i-1/2}, \sigma_{i+1/2}|\alpha_{i+1/2}|)] \tag{13c}$$

where $S = \operatorname{sgn}(\alpha_{i+1/2})$,

$$\sigma_{i+1/2} = \tfrac{1}{2}[1 - Q(v_{i+1/2})] \tag{13d}$$

and

$$\theta_i = |\alpha_{i+1/2} - \alpha_{i-1/2}|/(|\alpha_{i+1/2}| + |\alpha_{i-1/2}|). \tag{13e}$$

Correspondingly, the y-direction fluxes $\bar{G}_{i,j+1/2}^n$ and $\bar{G}_{i,j-1/2}^n$ are given by

$$\begin{aligned} \bar{G}_{i,j+1/2} = \tfrac{1}{2}\Bigg\{ & G(U_{i,j}) + G(U_{i,j+1}) \\ & - [G(U_{i,j+1}) - G(U_{i,j})]\, \frac{\Delta y_{j+1} - \Delta y_j}{\Delta y_{j+1} + \Delta y_j} \Bigg\} \\ & - \frac{1}{\lambda_j} \sum_{k=1}^{4} \beta_{i,j+1/2}^k R_{i,j+1/2}^k \end{aligned} \tag{14a}$$

$$\begin{aligned} \bar{G}_{i,j-1/2} = \tfrac{1}{2}\Bigg\{ & G(U_{i,j}) + G(U_{i,j-1}) \\ & - [G(U_{i,j}) - G(U_{i,j-1})]\, \frac{\Delta y_j - \Delta y_{j-1}}{\Delta y_j + \Delta y_{j-1}} \\ & - \frac{1}{\lambda_j} \sum_{k=1}^{4} \beta_{i,j-1/2}^k R_{i,j-1/2}^k \Bigg\} \end{aligned} \tag{14b}$$

In computing the y-direction flux, i is constant. Therefore, $\beta_{j+1/2}^k$ and $R_{j+1/2}^k$ are given by Eqs. (7) through (13) with i changed to j and u interchanged with v.

C. *Axisymmetric Case*

In Eqs. (4), the flux terms for axisymmetric problems are identical to those for planar problems, since the evaluation of the cell volume, flux area, and source term in the y-momentum equation take care of the geometric differences.

The algorithm presented in Eq. (5) is applied for both planar and axisymmetric flows using the proper construction of the flux area by appropriately considering the metric y^{α} in the equations of motion.

D. *Skewed Cells*

On any surface of a skewed cell, each of the four components of the flux vector [see Eq. (3)] is represented by two components, the x-component aligned with the x-coordinate direction and the y-component aligned with the y-coordinate direction. Once the four cells required for the flux calculations in each direction are determined (two upstream and two downstream of the cell surface being considered), the x-component flux is evaluated using Eq. (6) with the respective cell center values and locations and, similarly, the y-component is evaluated using Eq. (14). To determine these four cells, one must first locate the cells immediately upstream and downstream of this surface. The cell further upstream is determined by locating the cell connected to the surface opposite (upstream) to the surface under consideration. If there is more than one cell adjoining the upstream surface, the cell whose center is closer to the downstream cell center is selected. The further downstream cell is determined in a similar manner. The distances required to construct the flux corrector/limiters in Eqs. (6) and (14) are given by the projections of the cell and surface centers on the x-axis and y-axis, respectively. The scalar product of this flux vector and the surface normal yields the fluxes across $A_k N_{kx}$ and $A_k N_{ky}$. This procedure is very easy to implement and includes the case of using rectangular cells, either aligned or staggered, as in the test cases B and D of this paper as a degenerate case. However, if $N_{ky} \ll N_{kx}$, we may neglect the numerical viscosity and artificial compression in the y-direction flux calculation. This simplification is applied for the test case C calculation described in Section III.

III. Numerical Experiments

In order to verify the efficacy of the algorithm developed in the previous sections, the results of four numerical experiments are presented and compared to either exact solutions or detailed experimental measurements. These include two 1-dimensional, one 2-dimensional, and an axisymmetric flow.

A. *Riemann Problem (Case A)*

The Riemann problem for a polytropic gas ($\gamma = 1.4$), presented in Ref. [3], is reconsidered using both uniform and nonuniform grid systems as shown in the insert of Fig. 2.

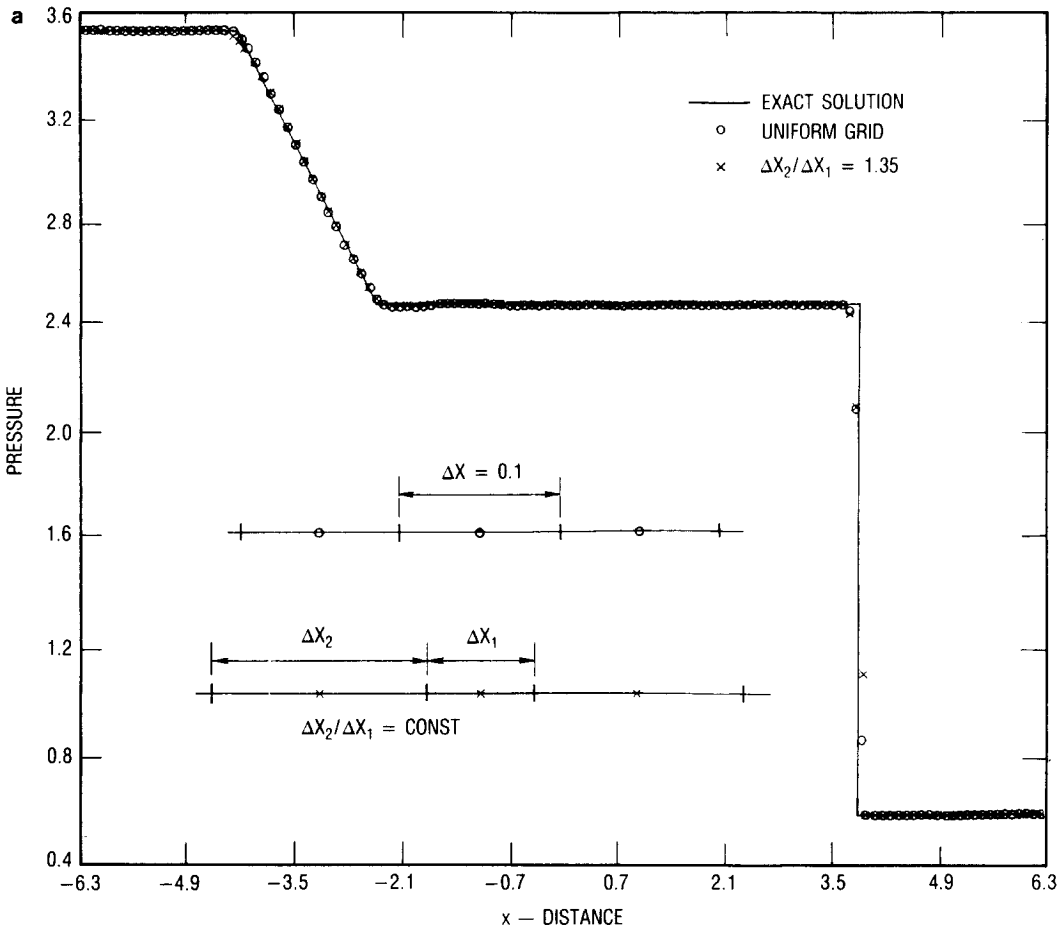

FIG. 2. Comparison of the calculated pressure variation for uniform and nonuniform cell distributions (Case A).

The initial conditions are given as

$$p = 3.52773, \quad \rho = 0.445, \quad u = 0.69888, \quad x < 0, \tag{15}$$

$$p = 0.571, \quad \rho = 0.5, \quad u = 0, \quad x > 0. \tag{16}$$

Comparisons of the respective pressure results obtained at corresponding flow times using uniform and nonuniform grids are shown in Figs. 2a–c. The exact solution is also shown for comparison purposes. Here, the cell size for the uniform grid was kept at $\Delta x = 0.1$. For the nonuniform grid, the cell size for cells 1, 3, 5, ... is set to Δx_1 and for cells 2, 4, 6, ... is set to Δx_2, where $\Delta x_1 + \Delta x_2 = 2\Delta x$. In this arrange-

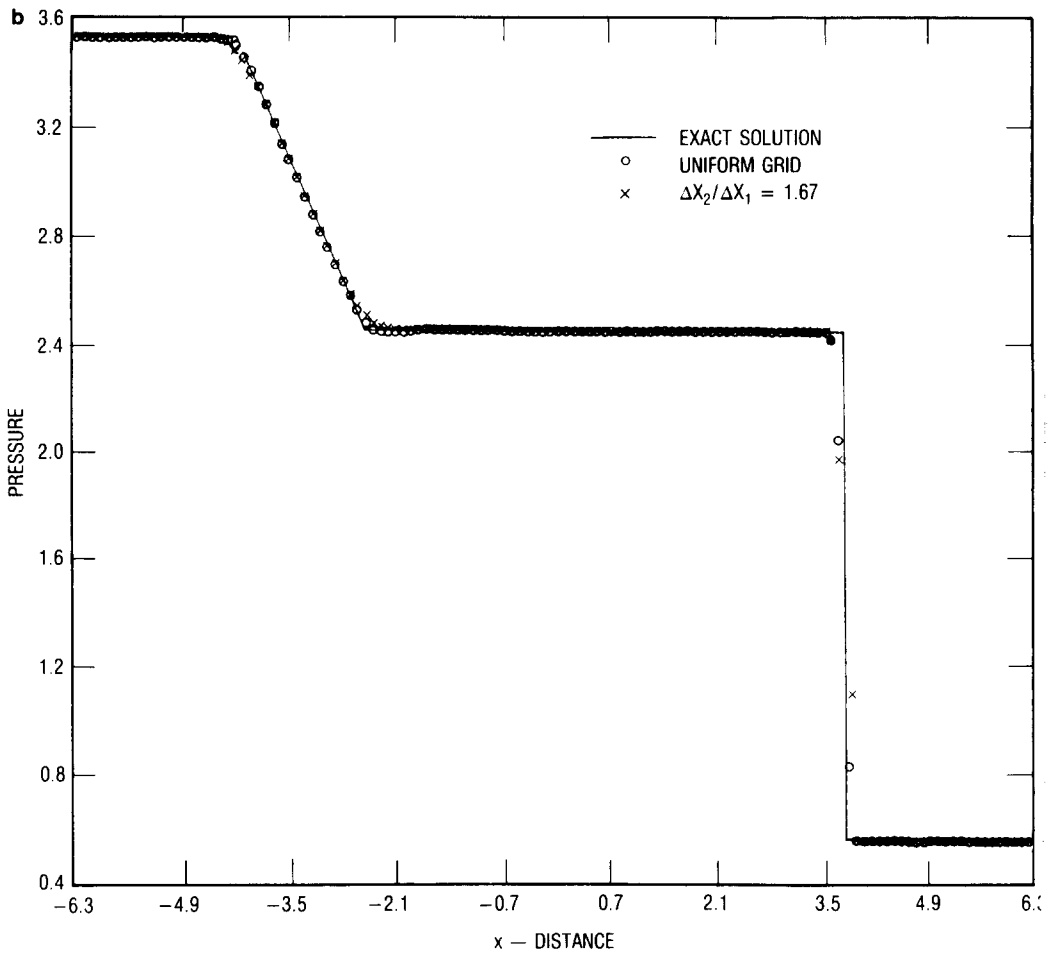

FIG. 2—*Continued*

ment, cell centers for both the uniform and nonuniform grid systems are coincident. For all calculations, the Courant number was kept constant at 0.9; ε (see Eq. (10)) was fixed at a value of 0.25.

Similar results were obtained for the density and velocity variations and demonstrate that the solutions derived from the present algorithm are insensitive to the nonuniformity of cell distribution up to at least a variation of $\Delta x_2/\Delta x_1 = 1.67$.

B. *Unsteady Flow in a Closed Shock Tube (Case B)*

Consider the initial/boundary value problem of a closed shock tube as depicted in Fig. 3a. Here, a diaphragm, located at $x = 0$, separates two gases at different

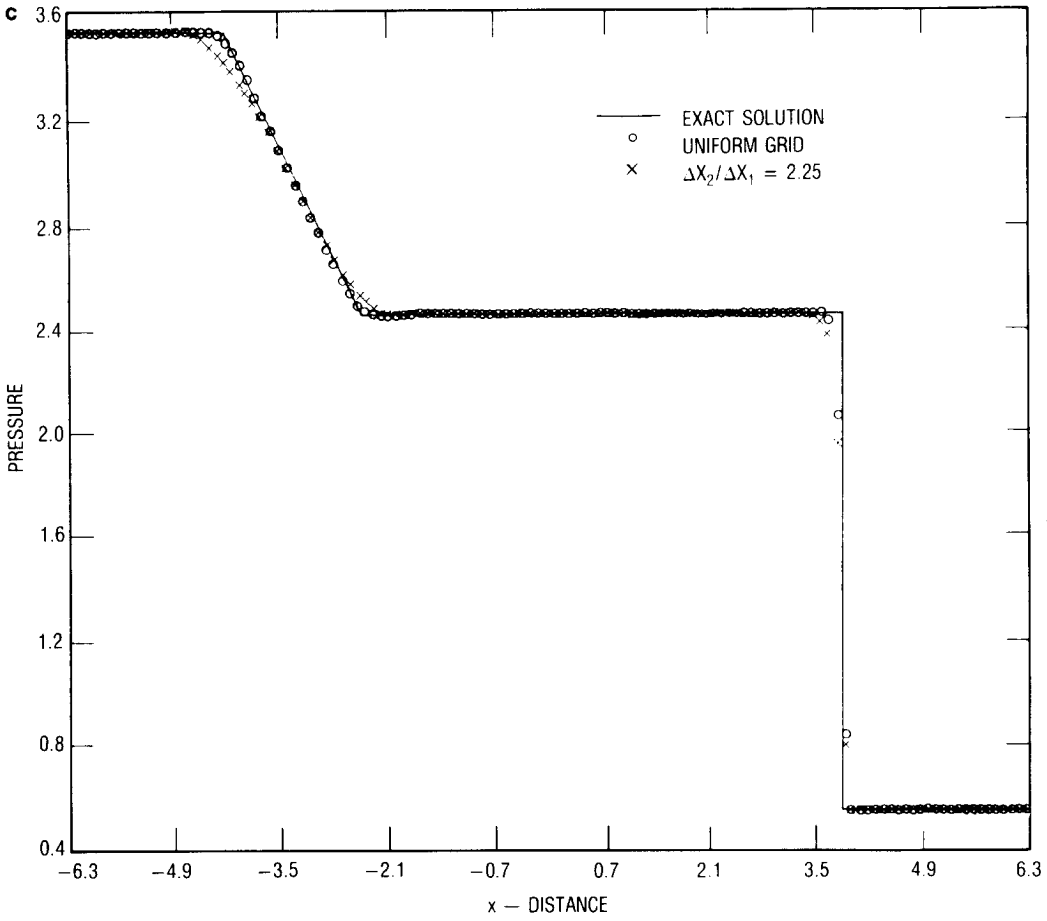

FIG. 2—*Continued*

conditions and is burst at $t=0$. The right and left end walls are located at ± 4.1, respectively; the calculation is carried on long enough for the waves to reflect off the walls ($\mathbf{u}\cdot\hat{N}=0$) and interact with the right running contact surface.

The exact solution to this problem is shown in Fig. 3b. Here, the rarefaction waves are schematically represented by broken lines. The interaction of the reflected shock and the contact surface takes place at $(x, t)=(3.2379, 2.5296)$. At this time, the leading front of the reflected rarefaction wave front (RRWF) is located to the left of $x=1.8897$. By approximating the continuous rarefaction fan with five characteristic lines, it can be shown that any interaction between the RRWF and the transmitted shock is very weak.

The present numerical simulation treats the problem in a 2-dimensional manner

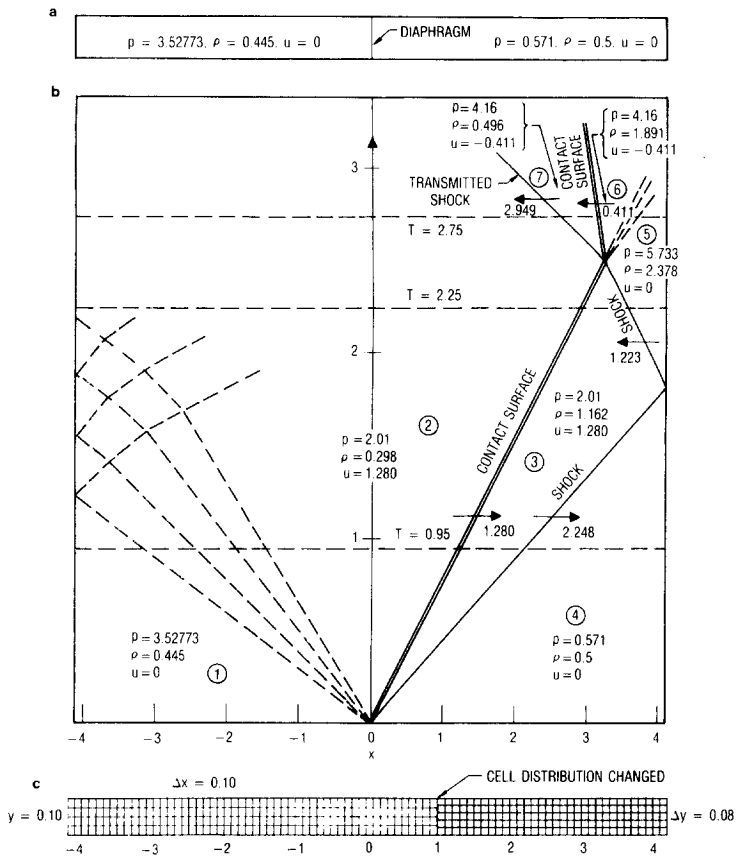

FIG. 3. Unsteady flow in a closed shock tube (Case B): (a) geometry and initial conditions; (b) exact solution; (c) computational cell distribution.

using the cell distribution shown in Fig. 3c. Notice that the cell distribution is changed at $x = 1$. The purpose of treating the problem in a 2-dimensional manner using this unnecessarily complicated cell distribution is to test the adaptability of the present algorithm to correctly handle cell interfaces which have interactions with more than one adjoining cell (e.g., at $x = 1$); see Section II.D.

The boundary condition on the solid end walls of the shock tube is

$$w_{nl} = \mathbf{u}_b \cdot \hat{N} = 0 \tag{17}$$

where $\mathbf{u}_b$ is the fluid velocity vector on the wall and $\hat{N}$ is the vector normal to the wall. Therefore, only the pressure on the wall contributes to the evaluation of the flux on this solid cell surface. This pressure is computed, in the manner suggested by Reddall [11], by treating the wall interaction as 1-dimensional wave reflections.

At $t = t^n$, the dependent variables ρ_n, p_n, and w_n are known, where $w_n = \mathbf{u} \cdot \hat{N}$ at the center of a cell adjacent to a solid boundary. For $w_n > 0$, the condition $w_{nl} = 0$ can be viewed as the result of a symmetric reflection of two shocks of equal strength; thus, the following equation can be derived [12] for the pressure, p_w, on the wall

$$\frac{p_w}{p_n} = 1 + \frac{\gamma(\gamma+1)}{4}\frac{w_n^2}{c_n^2}\left[1 + \sqrt{1 + \frac{16}{(\gamma+1)^2}\frac{c_n^2}{w_n^2}}\right], \tag{18}$$

where $c_n^2 = \gamma p_n/\rho_n$. For $w_n < 0$, the boundary condition $w_{nl} = 0$ is viewed as the result of an expansion wave propagating into the fluid from the solid surface. Using the Riemann invariant and isentropic relation, we can derive the equation

$$\frac{p_w}{p_n} = \left[1 + \frac{\gamma - 1}{2}\frac{w_n}{c_n}\right]^{2\gamma/(\gamma-1)} \tag{19}$$

for $w_n = 0$,

$$p_w = p_n. \tag{20}$$

In constructing the numerical viscosity and artificial compression contributions to the fluxes across the surface next to the solid wall, we need a cell outside the solid boundary. Here, the reflection principle is used to assign the cell center values for this fictitious cell.

Numerical results are shown in Figs. 4 through 6, where the CFL condition was fixed at 0.9 and $\varepsilon = 0.25$. Shown in Figs. 4a–c are the results for pressure, density, and velocity, respectively, before the shock reaches the right closed end. Notice that the shock is resolved in one or two cells. Figures 5a–c depict the results after the shock is reflected from the wall, and Figs. 6a–c depict the results following interaction of the reflected shock with the contact surface. It is especially important to note that the scheme correctly selected and captured the transmitted shock and reflected rarefaction wave. However, the first-order Godunov [13] technique cannot resolve these discontinuities. Also, note that at $t = 2.75$, the numerically captured transmitted shock location is at 2.5 ($\pm \Delta x = 0.1$) compared with the exact solution (assuming no interaction with RRWF) of 2.59. The agreement is excellent. The numerical solution indicates that a very weak interaction took place, which can be seen from the velocity profile, Fig. 6b. The interaction caused the maximum velocity to decrease from 1.280 to 1.240.

Included in Table I is a comparison of the exact solution for ρ, u, and p and that obtained using the present numerical scheme at locations in the $x - t$ plane as indicated by the circled numbers in Fig. 3b. The agreement is excellent and demonstrates the ability of the scheme to accurately capture weak and strong waves and discontinuities even after their interaction with the boundary surface and with each other. The results were not affected by the change in cell specification as

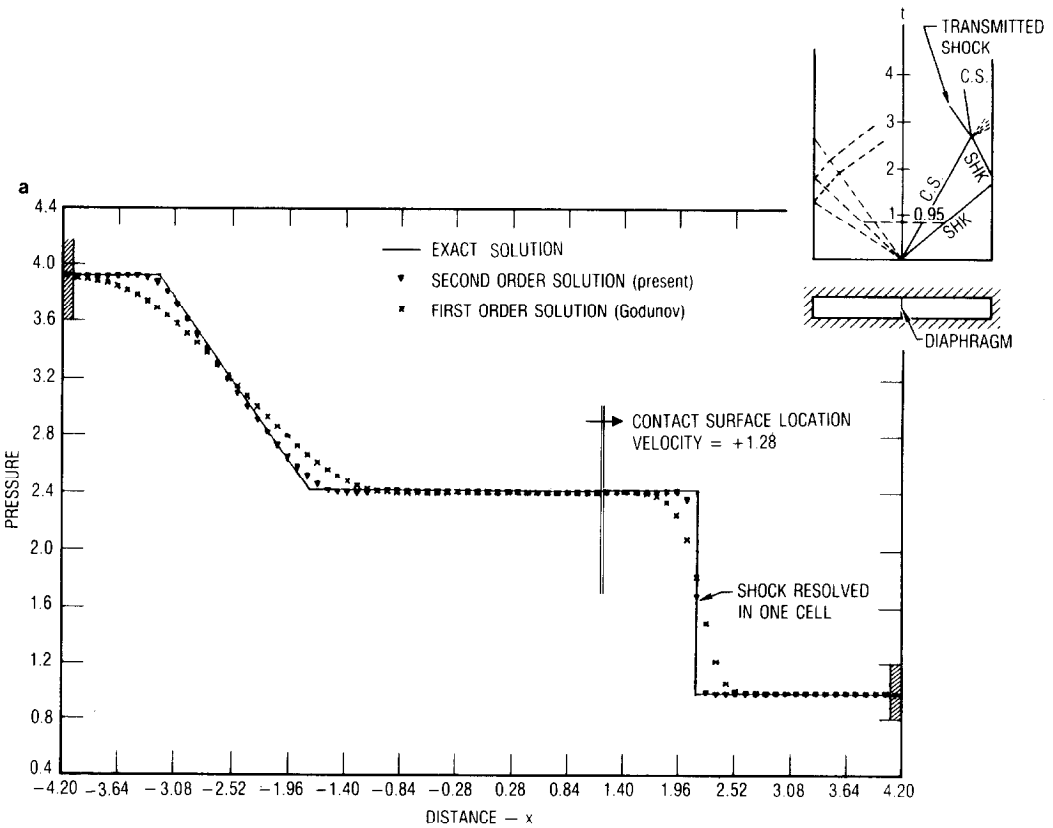

FIG. 4. Solution of the unsteady flow in a closed shock tube (Case B) at $t = 0.95$: (a) pressure distribution; (b) density distribution; (c) velocity distribution.

shown in Fig. 3a. The results also demonstrate the efficacy of the solid boundary treatment as well as the flux calculation at interfaces shared by more than two cells.

C. *Two-Dimensional, Steady Shock Reflection (Case C)*

Considered here is the problem of an oblique shock, generated by a supersonic flow over a sharp wedge, and the subsequent reflections from a flat plate located underneath the wedge and the wedge surface itself (see Fig. 7). The purpose of this exercise is to verify the accuracy of the present scheme using nonrectangular cells and the described method of handling solid surface boundary conditions.

A similar, but simpler, problem has been widely used as the test case for numerical schemes dealing with shocks [4–6]. In these computations [4–6], the initial oblique shock was generated by specifying a constant state corresponding to the desired shock strength and angle at some distance above the wall. Consequently, a

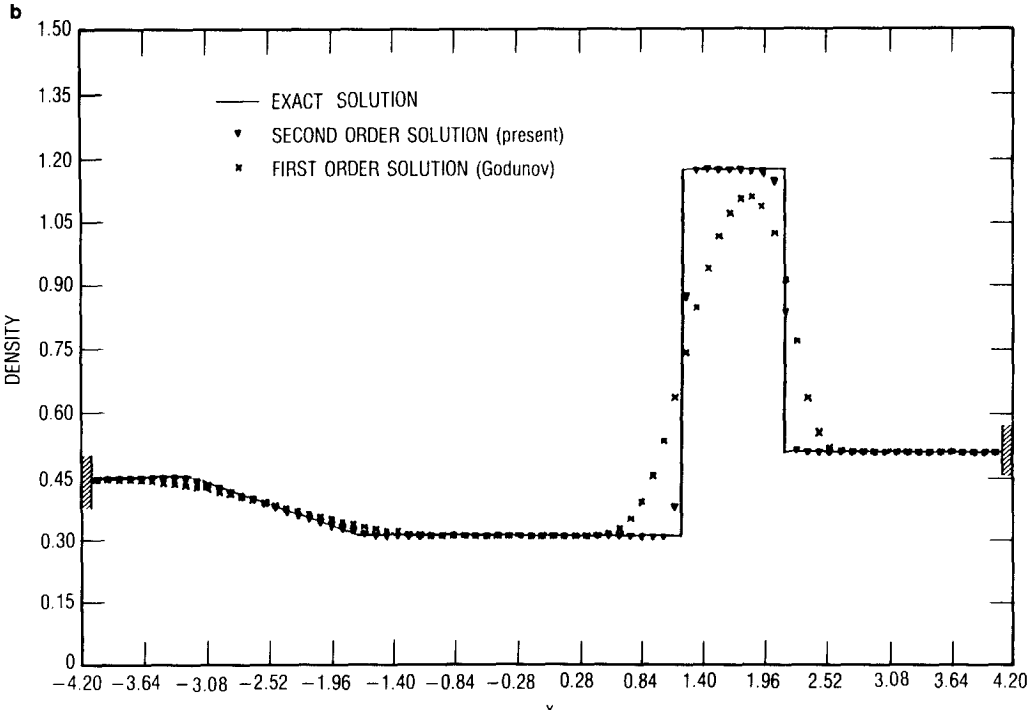

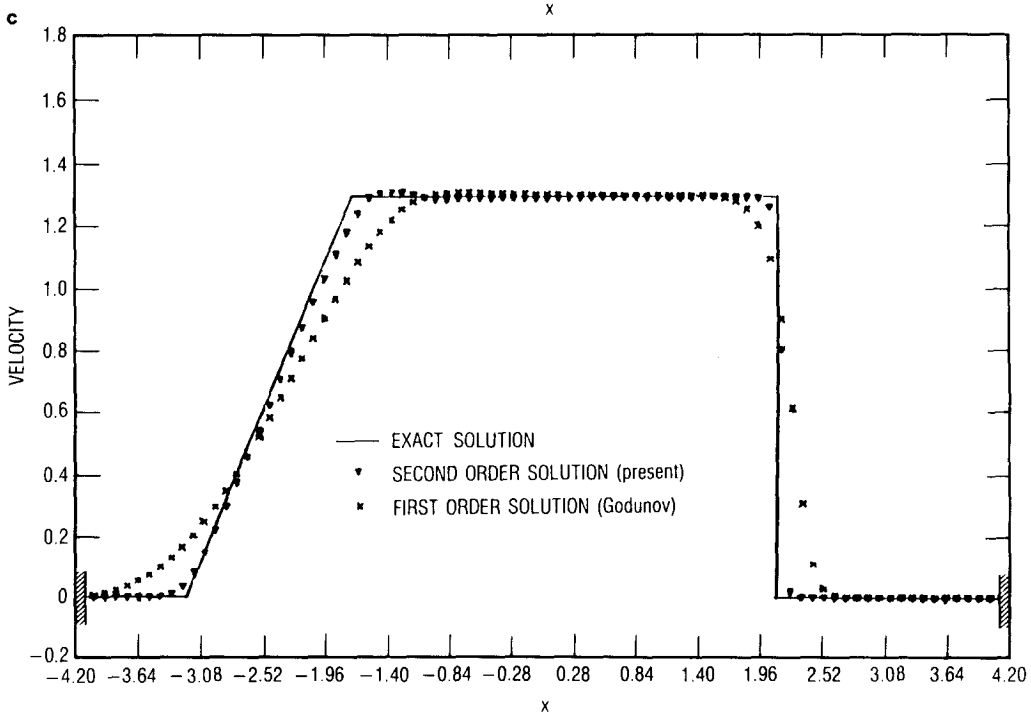

FIG. 4—*Continued*

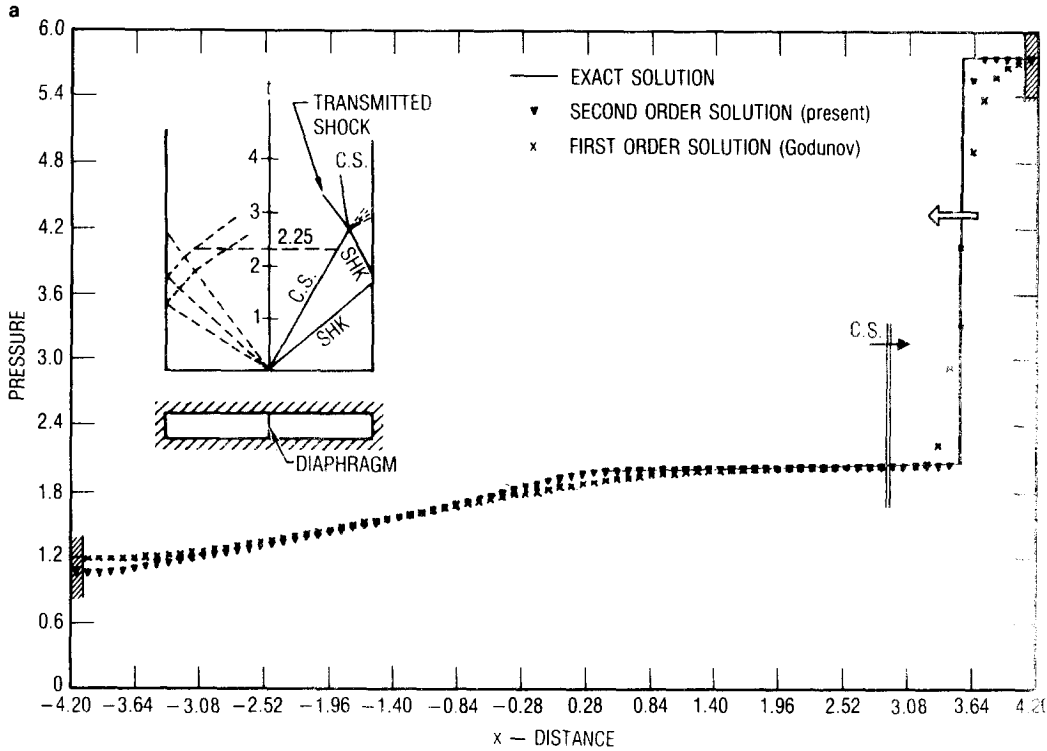

FIG. 5. Solution of the unsteady flow in a closed shock tube (Case B) at $t = 2.25$: (a) pressure distribution; (b) density distribution; (c) velocity distribution.

rectangular grid system was used in these simulations and the second reflection was omitted.

The cell distribution for the present calculation is shown in Fig. 7d, where it should be noted that—for other than the first four columns—the upper and lower surfaces of cells are not perpendicular to the y-axis and the cell inclinations are not equal.

The upstream condition is specified by prescribing the values of the variables at the cell center of each cell in the first column as indicated in Fig. 7. A zero-order extrapolation is used as the downstream condition, which results in the variables at the cell center of each cell in the last (N) column being set to the adjacent cell ($N-1$) values.

Calculations are performed with $\varepsilon = 0.25$ and a CFL condition of 0.9. Figs. 7b and c show the numerically determined pressure contours using, respectively, the present scheme and the first-order Godunov method [13] for the flux calculations. Notice that both methods predicted the correct pressure jump and shock angles; however, the shock captured by the Godunov scheme is excessively smeared. Care-

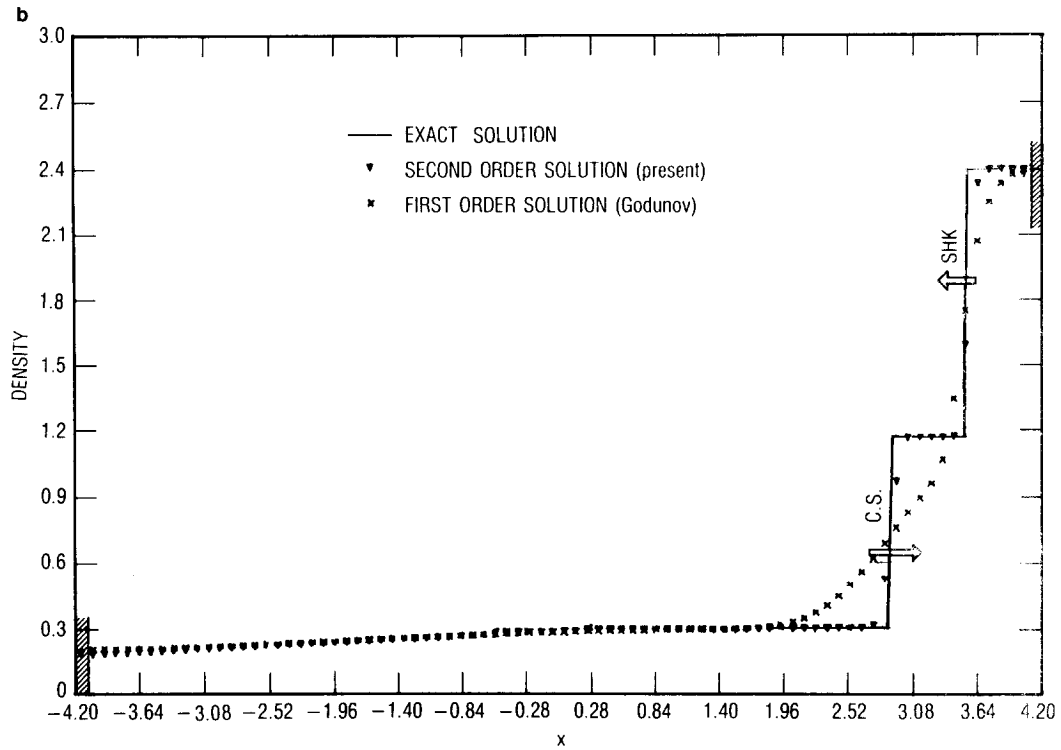

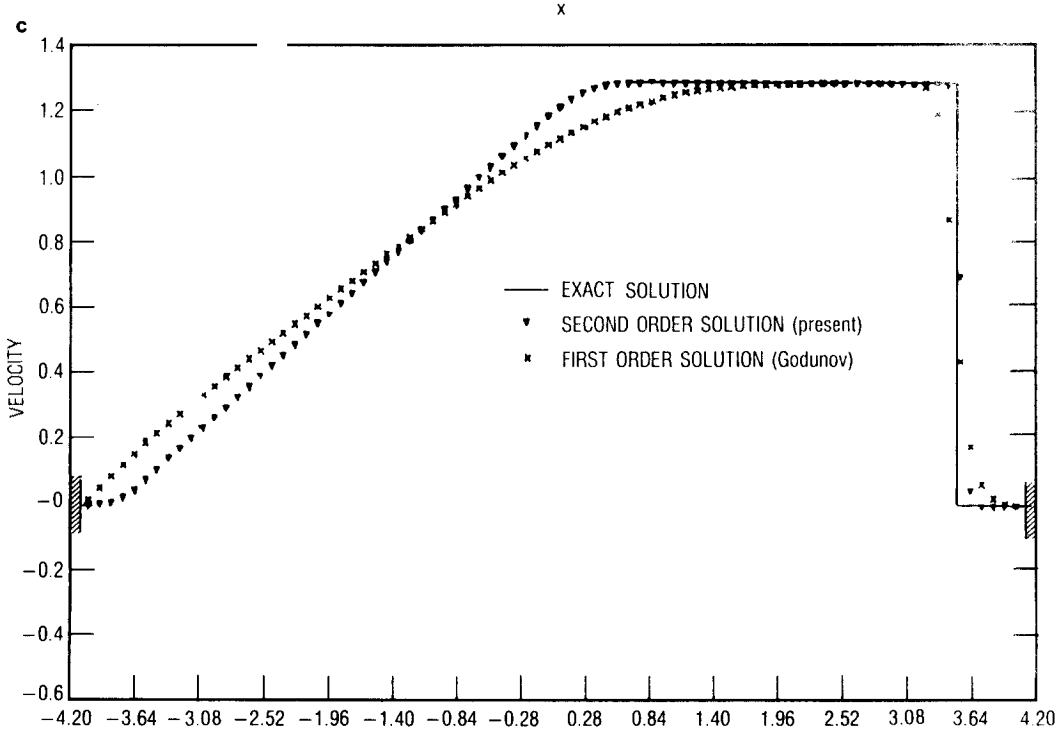

FIG. 5—*Continued*

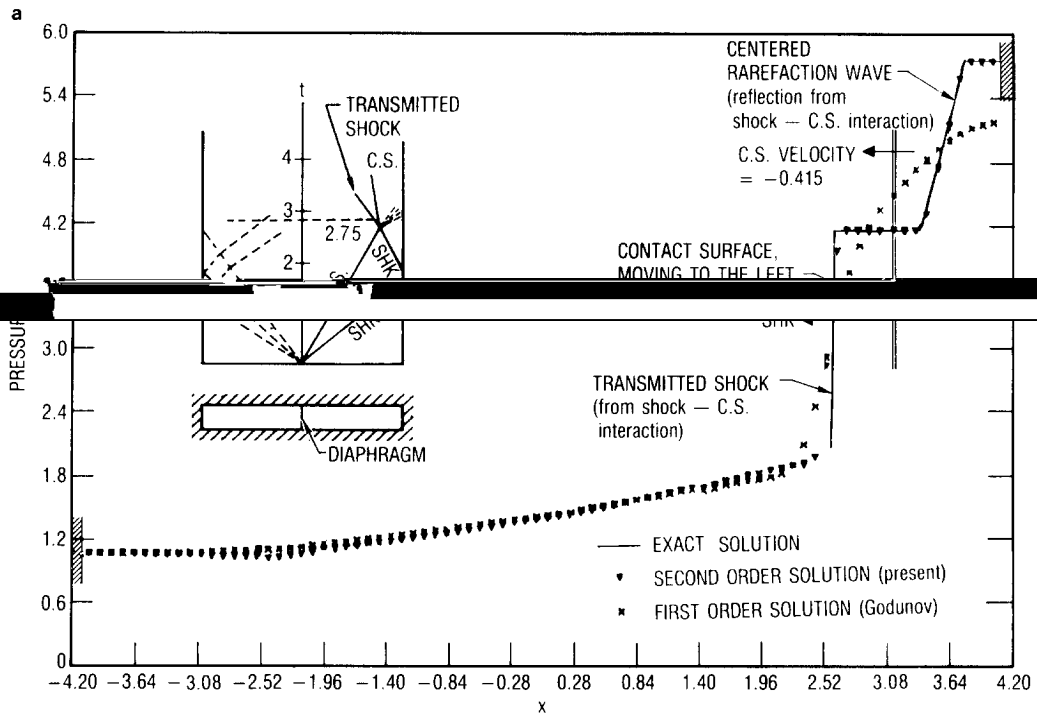

FIG. 6. Solution of the unsteady flow in a closed shock tube (Case B) at $t = 2.75$: (a) pressure distribution; (b) density distribution; (c) velocity distribution.

ful examination of the computational results obtained using the present scheme shows that the shocks are resolved in, at most, three cells.

D. *Blast Flowfield Generated by an Open-Ended Shock Tube (Case D)*

Consider the problem of a shock being expelled, at $t = 0$, from the open end of an axisymmetric shock tube (see Fig. 8a). Since the flow behind the shock is subsonic, a 2-dimensional rarefaction wave propagates into the tube. A blast wave, followed by an imbedded Mach disc, propagates downstream into the open space.

Numerical calculations have been performed using both uniform and very non-uniform cell distributions as shown in Figs. 8b and c. Schmidt and Duffy [14] carried out carefully designed experiments measuring the pressure time history at many locations upstream and downstream of the tube exit. High resolution spark shadowgraphs were also made. Detailed comparisons with these extensive data is the subject of another paper [15]; however, some sample results are included herein to demonstrate the results obtained. Figure 9 illustrates the pressure time history at a location on the centerline at $x = 1.5\,D$ to show the convergence of the scheme as the cell distribution is varied. In this figure, the measured pressure data

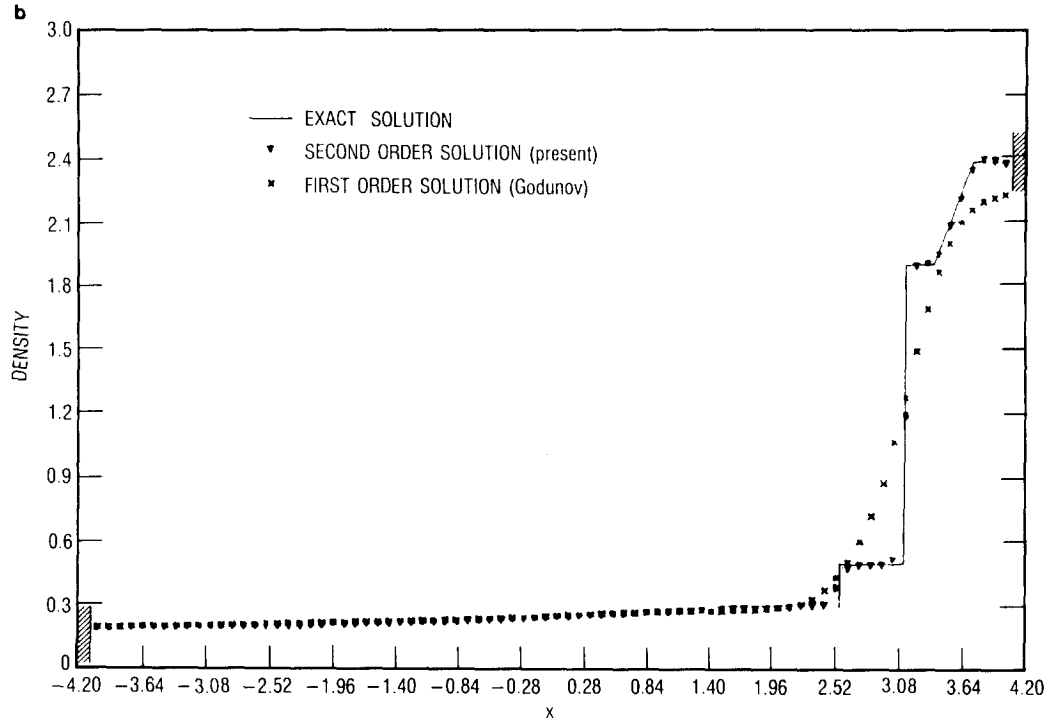

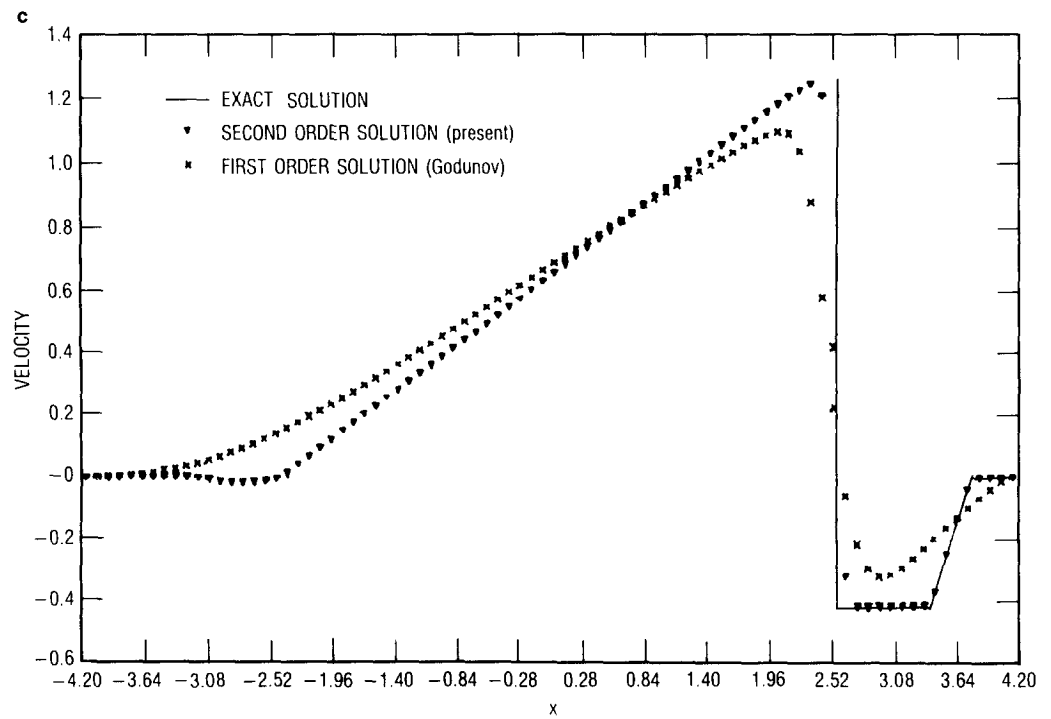

FIG. 6—*Continued*

TABLE I

Comparison of Exact and Numerical Solutions for the Unsteady Flow in a Closed Shock Tube (Case B)

Location	Variable	Numerical solution	Exact solution
2	P	2.014	2.010
	ρ	0.298	0.298
	u	1.281	1.280
3	P	2.014	2.010
	ρ	1.163	1.162
	u	1.281	1.280
5	P	5.758	5.733
	ρ	2.384	2.378
	u	0.0	0.0
6	P	4.165	4.160
	ρ	1.892	1.891
	u	−0.415	−0.411
7	P	4.165	4.160
	ρ	0.494	0.496
	u	−0.415	−0.411

are not reliable after $t = 1.2$ ms due to the interference of the instrument with the Mach disk moving downstream [16]. Figures 10a and b are, respectively, a pressure contour plot and a density contour plot from the numerical solution at $t = 1.5$ ms. Shown in Fig. 10c for comparison is a shadowgraph picture from experiments carried out without the pressure instrumentation in place taken at the corresponding time [16]. By overlaying these figures, using the Mach disk as a reference, it is seen that the main features of the complicated blast flowfield are all accurately reproduced in the numerical calculation (see Ref. [15] for quantitative details). These features include the Mach disk, jet shock, recompression shock, triple point, slip surface downstream of the triple point, vortex above the Mach disk, and the imbedded shock upstream of the vortex.

However, it was initially found that the rarefaction wave propagating upstream into the tube was severely suppressed when the artificial compression parameter θ_j was computed using Eq. (13e). A sensitivity study resulted in the development of the following representation for the compression parameter

$$\theta_j = 0.25\bar{\theta}_j + 0.75\bar{\theta}_j^{1.5}, \tag{21}$$

where $\bar{\theta}_j$ is defined by Eq. (13e). Use of this nonlinear form gave very good results for all waves and discontinuities, and it is used in the present scheme for all subsequent calculations.

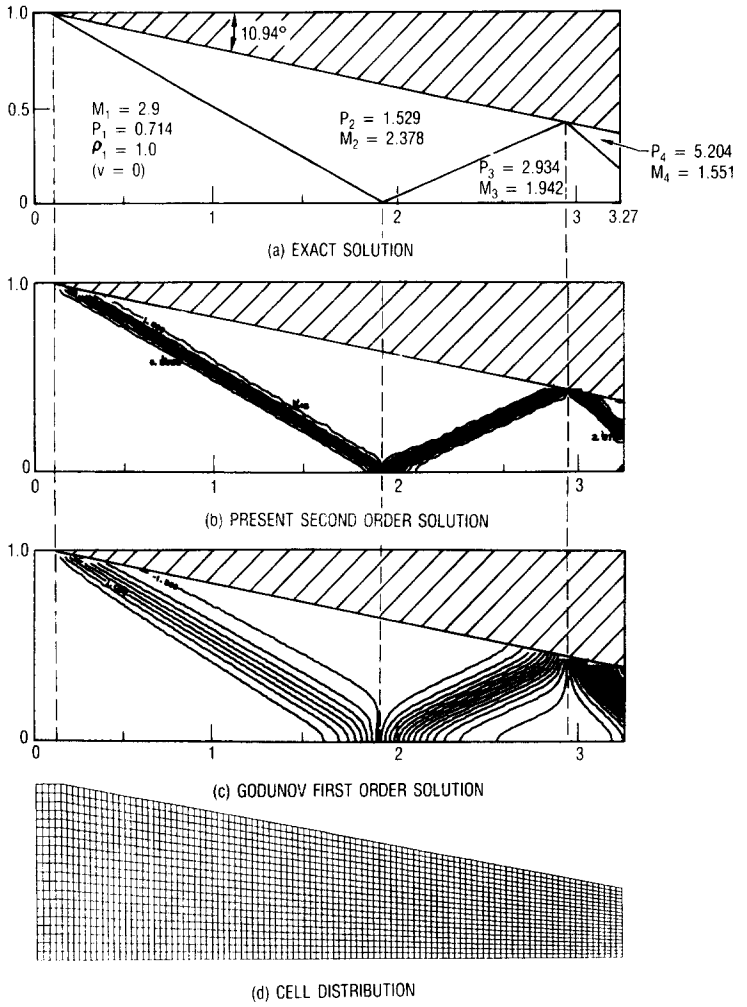

FIG. 7. Two-dimensional, steady shock reflection problem (Case C).

Solution of this very difficult time-dependent flow and the excellent comparisons [15] with experimental data verify the efficacy of the present technique, especially when a very highly variable cell distribution is used.

IV. CONCLUSIONS

A finite-volume TVD numerical algorithm, using nonuniformly distributed, skewed quadrilateral cells, has been developed for the solution of the Euler equa-

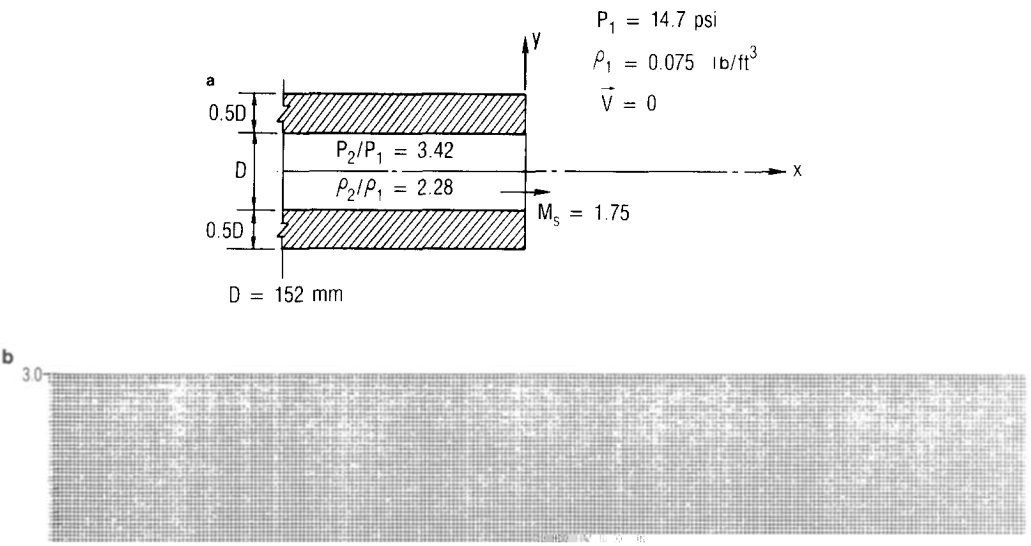

FIG. 8. Coordinates, initial conditions, and cell distributions for an axisymmetric blast flowfield problem (Case D): (a) coordinates and initial conditions; (b) uniform cell distribution (A); (c) highly nonuniform cell distribution (B).

tions. The TVD property is retained for nonuniform grid systems, and the method is second-order accurate. Four numerical examples have demonstrated the ability of the scheme to accurately resolve complicated wave patterns and interactions using highly nonuniform zonal cell distributions. The extension of the technique to three dimensions is straightforward and is presented in Ref. [1]. This extension uses the geometric flexibility already developed in Ref. [7] to treat any arbitrary zonal distribution of skewed quadrilateral cells and correctly handle the interaction of cell interfaces which bound multiple cells [18, 19]. This allows for the solution of very complicated geometries including moving bodies [18] and is very useful in the

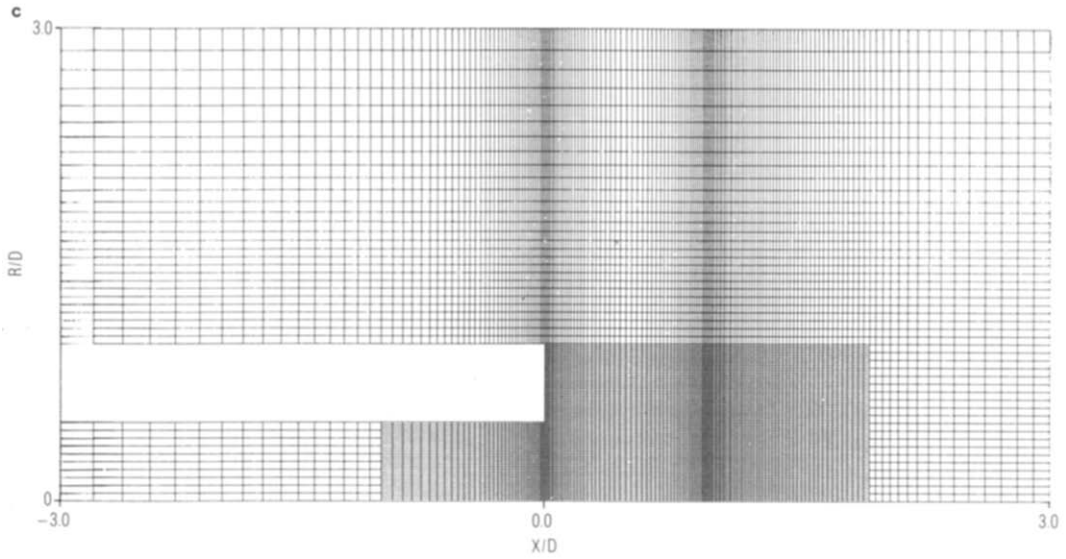

FIG. 8—*Continued*

application of multiblock cell specification, since cell nodal connectivity is not required in the present technique. This allows for local grid refinement without causing corresponding adverse effects (refinements) in other areas of the computational domain where they are not needed or desired.

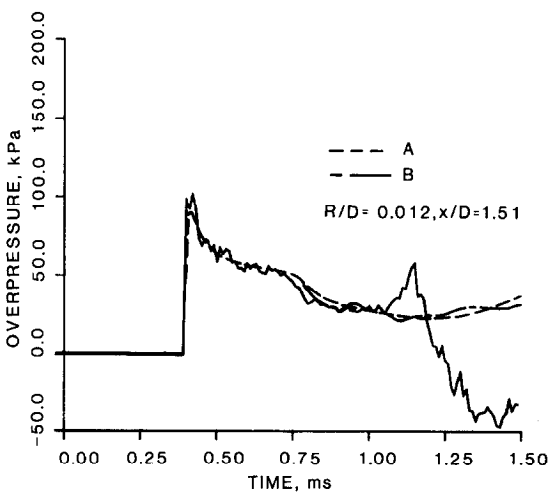

FIG. 9. Comparison of calculated and measured overpressure time history (Case D) at $X/D = 1.5$ ms.

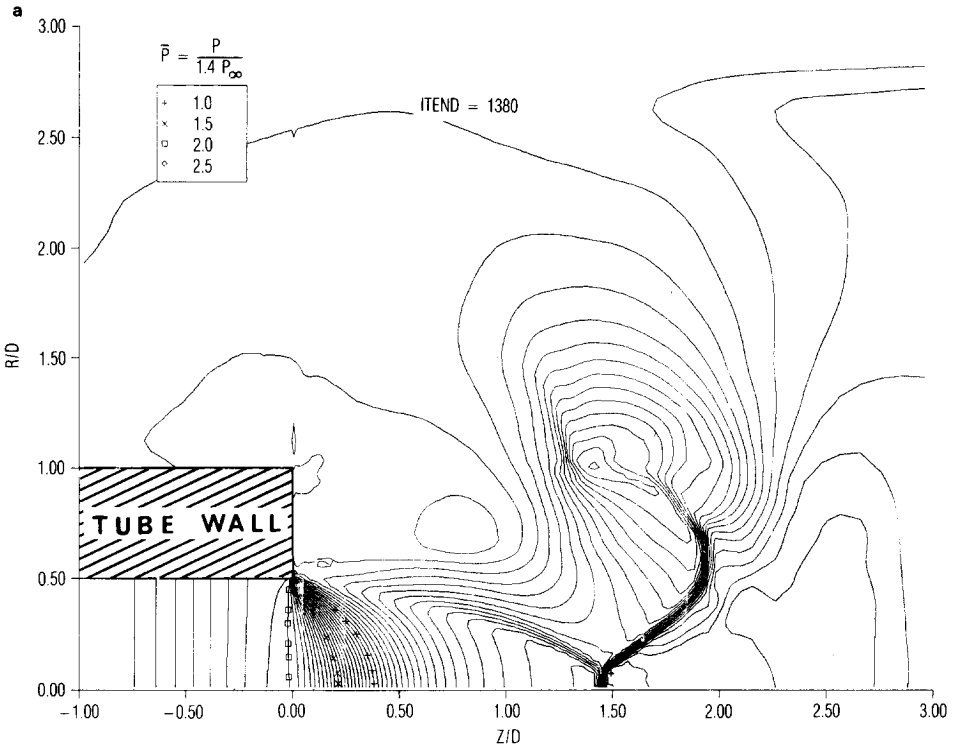

FIG. 10. Numerical simulation and experimental results for an axisymmetric blast flowfield (Case D) (using nonuniform cell distribution B): (a) pressure contour plot of numerical simulation at 1.5 ms; (b) density contour plot of numerical simulation at 1.5 ms; (c) shadowgraph [16] at 1.5 ms.

APPENDIX A: TVD PROPERTY FOR A NONUNIFORM GRID SYSTEM

Consider a 1-dimensional scalar hyperbolic equation in conservation form

$$\frac{\partial U}{\partial t} + \frac{\partial F(U)}{\partial x} = 0, \tag{A.1}$$

where $F(U)$ is a function of U and $a(U) = \partial F/\partial U$ is the characteristic speed. The numerical approximation to the solution of Eq. (A.1), by Eq. (5), can be written as

$$U_i^{n+1} = U_i^n - \lambda_i(\bar{F}^n_{i+1/2} - \bar{F}^n_{i-1/2}). \tag{A.2}$$

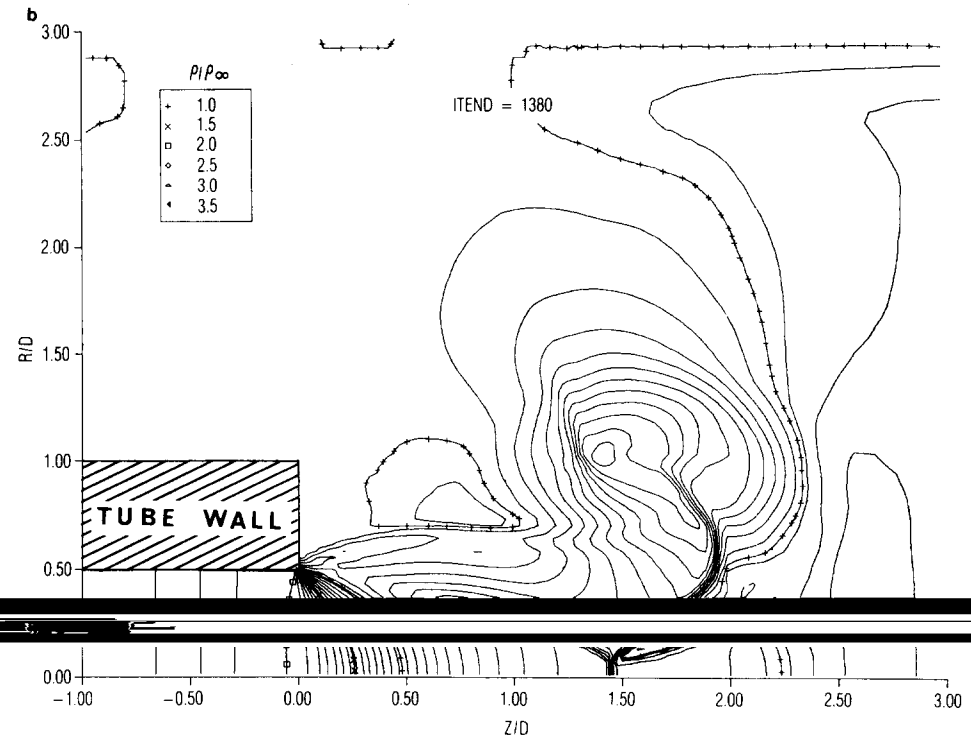

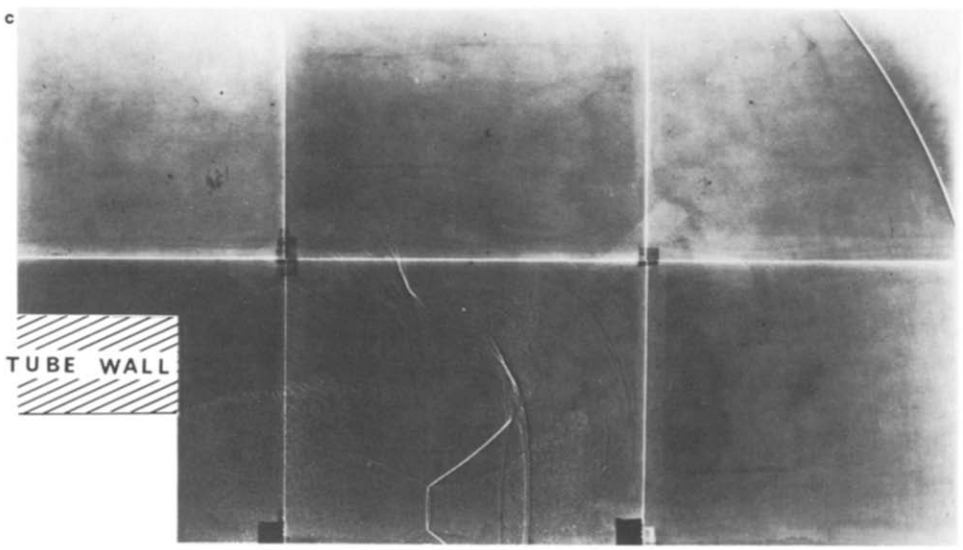

FIG. 10—*Continued*

The numerical fluxes, Eq. (6a), can be written as

$$\begin{aligned}\lambda_i \bar{F}_{i+1/2} &= F(U_i) + \tfrac{1}{2}[F(U_{i+1}) - F(U_i)] \\ &\quad - \frac{1}{2}[F(U_{i+1}) - F(U_i)] \frac{\Delta x_{i+1} - \Delta x_i}{\Delta x_{i+1} + \Delta x_i} + \frac{1}{2} Q_{i+1/2} \Delta_{i+1/2} U \\ &\approx \lambda_i f(U_i) - \frac{1}{2}\left[- \bar{\nu}_{i+1/2} \frac{\Delta x_i}{(\Delta x_{i+1} + \Delta x_i)/2} + Q_{i+1/2} \right] \Delta_{i+1/2} U \end{aligned} \tag{A.3}$$

and, similarly, Eq. (6b) can be written as

$$\lambda_i \bar{F}_{i-1/2} \approx \lambda_i f(U_i) - \frac{1}{2}\left[\bar{\nu}_{i-1/2} \frac{\Delta x_i}{(\Delta x_i + \Delta x_{i-1})/2} + Q_{i-1/2} \right] \Delta_{i-1/2} U, \tag{A.4}$$

where

$$\bar{\nu}_{i+1/2} = \lambda_i a_{i+1/2}, \qquad \bar{\nu}_{i-1/2} = \lambda_i a_{i-1/2}$$

and

$$a_{i+1/2} = \begin{cases} [f(U_{i+1}) - f(U_i)]/\Delta_{i+1/2} U & \text{when } \Delta_{i+1/2} U \neq 0 \\ a(U_i) & \text{when } \Delta_{i+1/2} U = 0. \end{cases} \tag{A.5}$$

Here

$$\Delta_{i+1/2} U \equiv U_{i+1} - U_i.$$

In Eq. (A.3), $Q_{i+1/2}$ represents the combination of the numerical viscosity and the artificial compression. However, the specific form of $Q_{i+1/2}$ is not required in the present analysis.

Using Eqs. (A.3) and (A.4), one can write Eq. (A.2) as

$$U_i^{n+1} = U_i^n + C_{+,i+1/2} \Delta_{i+1/2} U^n - C_{-,i-1/2} \Delta_{i-1/2} U^n, \tag{A.6}$$

where

$$C_{\pm,i+1/2} = \frac{1}{2}\left[Q_{i+1/2} \mp \bar{\nu}_{i+1/2} \left(1 \mp \frac{\Delta x_{i+1} - \Delta x_i}{\Delta x_{i+1} + \Delta x_i} \right) \right]. \tag{A.7}$$

Notice that Eq. (A.6) reduces to Eq. (3.5b) of Ref. [3] in a uniform grid system. Following Ref. [3], note that the proposed scheme—Eq. (A.2) with the numerical fluxes given by Eqs. (A.3) and (A.4)—is TVD if

$$C_{+,i+1/2} = \frac{1}{2}\left[Q_{i+1/2} - \bar{\nu}_{i+1/2} \left(1 - \frac{\Delta x_{i+1} - \Delta x_i}{\Delta x_{i+1} + \Delta x_i} \right) \right] \geqslant 0 \tag{A.8}$$

$$C_{-,i+1/2} = \frac{1}{2}\left[Q_{i+1/2} + \bar{\nu}_{i+1/2} \left(1 + \frac{\Delta x_{i+1} - \Delta x_i}{\Delta x_{i+1} + \Delta x_i} \right) \right] \geqslant 0 \tag{A.9}$$

and

$$C_{-,i+1/2} + C_{+,i-1/2} = \left[Q_{i+1/2} + \bar{v}_{i+1/2} \frac{\Delta x_{i+1} - \Delta x_i}{\Delta x_{i+1} + \Delta x_i} \right] \leqslant 1. \tag{A.10}$$

In the uniform grid system, conditions (A.8) through (A.10) can be satisfied sufficiently by taking

$$Q_{i+1/2} = Q(\bar{v}_{i+1/2}), \qquad |x| \leqslant Q(x) \leqslant 1 \tag{A.11}$$

under the CFL-like condition $\bar{v}_{i+1/2} < \mu \leqslant 1$. Here, μ is a constant.

Note that in the nonuniform grid system conditions, Eqs. (A.8) through (A.10) are satisfied if

$$Q_{i+1/2} = Q(x), \qquad |x| \leqslant Q(x) \leqslant \mu, \tag{A.12}$$

where

$$x = \bar{v}_{i+1/2} \left[1 + \frac{|\Delta x_{i+1} - \Delta x_i|}{\Delta x_{i+1} + \Delta x_i} \right] \tag{A.13}$$

and

$$\mu = 1/[1 + |\Delta x_{i+1} - \Delta x_i|/(\Delta x_{i+1} + \Delta x_i)]. \tag{A.14}$$

In comparison with the analysis of Ref. [3], the effect of grid nonuniformity on the TVD property is of the order $(\Delta x_{i+1} - \Delta x_i)/(\Delta x_{i+1} + \Delta x_i)$. As shown in Appendix B, this is the same order of magnitude as the truncation error when the $F(U)$ term is differenced. Therefore, the $Q_{i+1/2}$ term is constructed using the formula given in Ref. [3] for the uniform grid system (provided $\bar{v}_{i+1/2}$ is evaluated using the local grid size Δx_i). A formal truncation error analysis of this method of constructing $Q_{i+1/2}$ term has not been carried out. However, Case A of the numerical experiments was performed to evaluate this approach. This example demonstrated that the proposed method will not produce noticeable effects if the ratio of the sizes of two adjacent cells is less than 1.67. One can used this ratio as a qualitative guide.

APPENDIX B: On The Truncation Error

As shown in Appendix A, the nonuniform grid system modification required to preserve the TVD property is of order $(\Delta x_{i+1} - \Delta x_i)/(\Delta x_{i+1} + \Delta x_i)$. By substitution of Eqs. (A.3) and (A.4) into Eq. (A.2) and use of a Taylor series expansion, the

truncation error of the main flux term (excluding the numerical viscosity, $Q=0$) can be evaluated. This yields

$$\frac{\partial U}{\partial t}+\frac{\partial F}{\partial x}+\mathrm{TER}=0, \tag{B.1}$$

where TER denotes the truncation error. The "leading" term of TER is

$$\mathrm{TER}=\frac{1}{4}\left(\frac{\partial^2 F}{\partial x^2}\right)(l_{i+1}-l_i)+O(l_{i+1}^2, l_i^2), \tag{B.2}$$

where $l_{i+1}=1/2(\Delta x_{i+1}+\Delta x_i)$ and $l_i=1/2(\Delta x_i+\Delta x_{i-1})$ are the distances between cell i and adjacent cells.

For an algebraic grid distribution [10],

$$\begin{aligned} r_i &= l_{i+1}/l_i = 1+O(l^p)\ P>0 \\ l &= \max_i l_i < 1. \end{aligned} \tag{B.3}$$

By Eq. (B.3), the larger the p, the smoother is the grid distribution. It is concluded that

$$\mathrm{TER}\sim O(l_i l^p)+O(l_{i+1}^2 l_i). \tag{B.4}$$

Thus, for $p>1$, the present finite volume scheme for nonuniform cell distributions is second order.

It is worth noting that since the cell center value is used for the volume integral, interpreting the integration procedure as an application of the trapezoidal rule, the truncation error associated with this integration is of the order (l_i^3).

ACKNOWLEDGMENT

Part of this work was supported by the U.S. Army Ballistic Research Laboratories under Contract F04701-85-C-0086-P00016.

REFERENCES

1. B. VAN LEER, *J. Comput. Phys.* **32**, 101 (1979).
2. S. OSHER AND F. SOLOMON, *Math. Comput.* **38**, 339 (1982).
3. A. HARTEN, *J. Comput. Phys.* **49**, 357 (1983).
4. H. C. YEE, R. F. WARMING, AND A. HARTEN, *J. Comput. Phys.* **57**, 327 (1985).
5. S. R. CHARKRAVARTHY AND S. OSHER, AIAA-83-1943, July 1983 (unpublished).
6. P. COLELLA, Lawrence Berkely Lab. Report 17023, May 1983 (unpublished).
7. J. C. T. WANG, J. C. BUELL, AND G. F. WIDHOPF, "A Generalized Three-Dimensional Inviscid Flow Field Code Using the Godunov Method (3DGENGOD), Part I, Theory and Application," The Aerospace Corporation, El Segundo, CA (unpublished).

8. S. K. GODUNOV, A. V. ZABIODIN, AND G. P. PROKOPOV, *Comput. Math. Math Phys.* 1187 (1961).
9. P. L. ROE, *J. Comput. Phys.* **43**, 357 (1981).
10. E. TURKEL, ICASE Report No. 85-43, Sept. 1985 (unpublished).
11. W. REDDALL, private communication.
12. R. COURANT AND K. O. FREDRICKS, "Supersonic Flow and Shock Waves," *Pure and Applied Mathematics Vol. 1* (Interscience, New York, 1948).
13. G. F. WIDHOPF, J. C. BUELL, AND E. M. SCHMIDT, AIAA-82-0973, June 1982 (unpublished).
14. E. M. SCHMIDT AND S. DUFFY, AIAA-85-0049, Jan. 1985 (unpublished).
15. J. C. T. WANG AND G. F. WIDHOPF, AIAA-87-1320, June 1987 (unpublished).
16. E. SCHMIDT, USA Ballistic Research Laboratory, Aberdeen Proving Ground, Aberdeen, MD, private communication.
17. J. C. T. WANG, G. F. WIDHOPF AND S. H. CHEN, AIAA-88-0228, Jan. 1988 (unpublished).
18. J. C. BUELL AND G. F. WIDHOPF, AIAA-84-1641, June 1984 (unpublished).
19. J. C. BUELL, AIAA-84-1629, June 1984 (unpublished).